

# Characteristics of Station-Derived Convective Cold Pools Over Equatorial Africa

Jannik Hoeller<sup>1,2</sup>, Jan O. Haerter<sup>1,2,3,4</sup>, Nicolas Da Silva<sup>1</sup>

<sup>1</sup>Integrated Modeling, Leibniz Centre for Tropical Marine Research, Fahrenheitstr. 6, 28359 Bremen, Germany

<sup>2</sup>Niels Bohr Institute, Copenhagen University, Blegdamsvej 17, 2100 Copenhagen, Denmark

<sup>3</sup>Physics and Earth Sciences, Constructor University Bremen, Campus Ring 1, 28759 Bremen, Germany

<sup>4</sup>Department of Physics and Astronomy, University of Potsdam, Karl-Liebknecht-Straße 32, 14476 Potsdam, Germany

## Key Points:

- 4289 cold pools are identified across equatorial Africa based on temperature and wind criteria.
- The occurrence and intensity of the observed cold pools are related to low-level moisture conditions and the depth of convection.
- The identified cold pool gust fronts closely correlate with satellite-observed brightness temperature discontinuities.

---

Corresponding author: Jannik Hoeller, [jannik.hoeller@leibniz-zmt.de](mailto:jannik.hoeller@leibniz-zmt.de)

**Abstract**

Due to their potential role in organizing tropical mesoscale convective systems, a better understanding of cold pool (CP) dynamics in such regions is critical, particularly over land where the diurnal cycle further concentrates convective activity. Numerical models help disentangle the processes involved but often lack observational benchmark studies. To close this gap, we analyze nearly 43 years of five-minute resolution near-surface timeseries records from twelve automatic weather stations across equatorial Africa. We identify 4289 CPs based on criteria for temperature and wind. The identified CP gust fronts, which exhibit respective median temperature and specific humidity decreases of  $5.2\text{ K}$  and  $2.8\text{ g/kg}$ , closely correlate with satellite-observed brightness temperature discontinuities. Despite weak diurnal variation in precipitation, observed CP occurrence shows a pronounced diurnal cycle with an afternoon peak — a finding we attribute to low-level moisture conditions. Our findings can serve as observational benchmark to improve simulations of CP organization.

**Plain Language Summary**

Convective cold pools form when rain evaporates underneath thunderstorm clouds. The evaporation causes the air to cool and sink toward the ground, where it is deflected horizontally. Cold pools are thus associated with strong gusty winds, and over tropical land, they can be especially vigorous. Cold pools are also suggested to contribute to the organization of thunderstorm clouds into large clusters of rain-producing areas. The widespread, heavy rainfall can then cause flooding. To better predict such flooding in numerical weather models, having a precise observational basis for cold pool properties is essential — yet currently missing in equatorial Africa. We here provide such an observational benchmark by analyzing thousands of cold pools using timeseries of near-surface temperature, wind, humidity and precipitation. We additionally show that the cold pools can even be detected from satellite data when analyzing abrupt changes in cloud top temperature. Such satellite-based detection could open for cold pool studies across all tropical land areas — of great practical relevance to the prediction of thunderstorm clusters.

**1 Introduction**

Convective cold pools (CPs) are caused by the evaporation of rainfall beneath deep convective clouds (Zuidema et al., 2017). The resultant denser air volume within the sub-cloud layer spreads out laterally along the surface and is known to cause a so-called "gust front" along its edges. The gust front features strong horizontal and vertical winds along with moisture and temperature anomalies which together can give rise to additional deep convective events, e.g., under collisions (Purdom, 1976; Feng et al., 2015). CPs are thus important agents in mediating interactions between deep convective cells and thus the self-organization of thunderstorm systems (Simpson, 1980; Tompkins, 2001b; Haerter et al., 2019; Jensen et al., 2021).

Recent idealized cloud-resolving and large-eddy simulations have provided new quantitative and qualitative insight into CP structure and dynamics, such as scaling analysis to obtain a required mesh resolution (Fiévet et al., 2022), the potential origin of moisture rings (Langhans & Romps, 2015; Drager et al., 2020), and insight into interaction mechanisms (Tompkins, 2001a; Torri et al., 2015; Meyer & Haerter, 2020; Haerter et al., 2020). Such simulation studies have also triggered a range of simplified conceptual models, (Böing, 2016; Haerter, 2019; Haerter et al., 2019; Nissen & Haerter, 2021; Niehues et al., 2022), which may help elucidate some of the organizing mechanisms involved. New methods of CP detection in numerical studies have also been developed, which help automatize the tracking of CP gust fronts and their interactions in space and time (Gentine et al., 2016; Torri & Kuang, 2019; Fournier & Haerter, 2019; Henneberg et al., 2020; Hoeller et al., 2022; Hoeller, Fiévet, & Haerter, 2023).

67 Despite this progress in numerical and theoretical work, direct measurements of CPs  
 68 are still limited to specific geographic regions, such as the tropical and sub-tropical ocean  
 69 (Zipser, 1977; Zuidema et al., 2012; Vogel, 2017; Chandra et al., 2018; Vogel et al., 2021),  
 70 and mid-latitude continental regions in Central Europe (Kirsch et al., 2021; Kruse et al.,  
 71 2022) or North America (Mueller & Carbone, 1987; Wakimoto, 1982; Engerer et al., 2008;  
 72 Hitchcock et al., 2019; van den Heever et al., 2021). With a focus on dust storms, in semi-  
 73 arid tropical regions a CP detection method was suggested based on surface measure-  
 74 ments and satellite microwave data (Redl et al., 2015).

75 The importance of collecting information on CPs and precipitation in deep tropi-  
 76 cal regions has been pointed out (Adams et al., 2015) but systematic, climatological stud-  
 77 ies on CPs in such regions are still rare or lacking. This may partially be due to diffi-  
 78 cult environmental conditions which pose challenging demands on equipment and main-  
 79 tenance (Parker et al., 2008). Also the availability of funds may hinder systematic long-  
 80 term campaigns in some regions. A notable exception is the trans-African hydro-meteorological  
 81 observatory (TAHMO) which offers a promising network of station measurements in many  
 82 sub-Saharan African countries (van de Giesen et al., 2014). Using a range of stations from  
 83 the TAHMO network, we here present a climatology of CP measurements for equato-  
 84 rial Africa and compare findings to previous work in other geographic regions.

## 85 2 Data

### 86 2.1 Station data

87 We utilize data from twelve ATMOS41 automatic weather stations (AWS) in equa-  
 88 torial Africa (Fig. 1), operated by TAHMO (TAHMO, 2023). The stations are situated  
 89 in Cameroon, the Democratic Republic of the Congo (DR Congo), Nigeria, and Uganda.  
 90 In order to investigate the influence of regional climatic differences on CPs, we group sta-  
 91 tions according to their respective deployment countries in the following analysis.

92 The AWS provide data at a temporal resolution of five minutes. All stations are  
 93 installed at an approximate height of two meters above the surface. For our analysis, we  
 94 employ the station records of precipitation, atmospheric pressure, air temperature, rel-  
 95 ative humidity, and wind gust speed. To derive the wind gust speed, the ATMOS41 mea-  
 96 sures the instantaneous wind speed every ten seconds and outputs the maximum instan-  
 97 taneous wind speed value within the corresponding five-minute interval as wind gust speed.  
 98 If an instantaneous wind speed is larger than eight times the running average of the pre-  
 99 vious ten instantaneous measurements, the measurement is rejected. While this method  
 100 may prevent spurious spikes in the wind record under normal conditions, it can cause  
 101 missing wind data in cases of large and sudden wind changes. Given the frequent occur-  
 102 rence of such strong wind variations associated with CP gust fronts, approximately 22%  
 103 of all identified CPs have an incomplete wind record.

104 We analyze the data recorded by the stations from January 1, 2019, to September  
 105 30, 2023. As not all stations were operational throughout the entire period, we limit our  
 106 analysis for each station to days with complete air temperature record. Additionally, we  
 107 require the air temperature to be recorded for a minimum of ten consecutive minutes from  
 108 the previous day and for the subsequent 120 minutes on the following day. The result-  
 109 ing number of analysis days per station is indicated in Fig. 1. In total, we analyzed 15602  
 110 days and thus nearly 43 years of station data.

111 Based on the station-measured variables, we additionally compute both mixing ra-  
 112 tio,  $r$  and saturated mixing ratio,  $r_{sat}$  (see Text S1), and derive the mixing ratio deficit,  
 113  $r_D \equiv r_{sat} - r$  and the specific humidity,  $q \equiv r/(1 + r)$ .

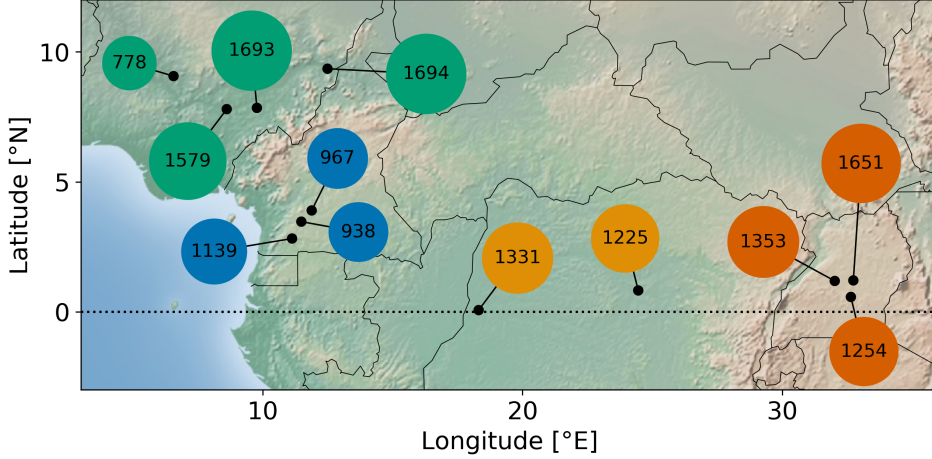


Figure 1: **Employed weather station data.** Map of equatorial Africa with station locations (filled black circles) utilized in this study. Numbers represent available days of station data with a complete record of air temperature,  $T$ . The stations are grouped into four regions denoted by the colored circles: Cameroon (blue), Democratic Republic of the Congo (yellow), Nigeria (green), Uganda (red). The area of colored circles is proportional to the available days of station data.

114 **2.2 Satellite data**

115 Apart from the station data, we utilize infrared brightness temperature measure-  
 116 ments which we derive from satellite-measured effective radiances. The radiances are ex-  
 117 tracted from Meteosat Second Generation (MSG) 0° products provided by the European  
 118 Organisation for the Exploitation of Meteorological Satellites (EUMETSAT) (EUMETSAT,  
 119 2023). The data has a baseline repeat cycle of 15 *min* and a spatial resolution of 3 *km*  
 120 in the sub-satellite point. To convert the radiances to brightness temperatures we em-  
 121 ploy equation 5.3 and the corresponding regression coefficients of EUMETSAT (2012).

122 **3 Methods**

123 **3.1 Cold Pool Detection Algorithm**

124 (i) **Temperature criterion.** A potential CP event is detected at a given time  $t$  if three  
 125 conditions apply: similar to Kirsch et al. (2021) we require a substantial temperature  
 126 decrease  $\Delta T \leq -2 K$ , within the 20 *min* window from  $t - 5 \text{ min}$  to  $t + 15 \text{ min}$ . Ad-  
 127 ditionally, we require the decrease of  $\Delta T$  to be monotonic and  $T(t) - T(t - 5 \text{ min}) \leq$   
 128  $0.5 K$ .

(ii) **Wind criterion.** To verify detected potential CP events, we adapt the wind cri-  
 terion introduced by Kruse et al. (2022). For this purpose, we compute the wind gust  
 anomaly for each time  $t$  as

$$\Delta u_g(t) \equiv u_g(t) - \bar{u}_g(t), \quad (1)$$

129 where  $u_g$  is the wind gust speed and  $\bar{u}_g$  its centered 2-hour running mean, i.e., the mean  
 130 value of the 25 wind gust speeds recorded during the the corresponding 2-hour window.

For a potential CP event at time  $t$  we identify the maximum wind gust anomaly,  
 $\Delta u_g^{max}$ , between  $t - 20 \text{ min}$  and  $t + 40 \text{ min}$ . We consider it as CP event if

$$\Delta u_g^{max} \geq \overline{\Delta u_g}(t) + 3 \sigma_{\Delta u_g}(t), \quad (2)$$

131 with the centered 24-hour running mean of the wind gust anomaly,  $\overline{\Delta u_g}$ , and the cor-  
 132 responding 24-hour running standard deviation,  $\sigma_{\Delta u_g}$ .

133 As the CP onset is defined based on the temperature criterion, we also search for  
 134 associated wind gusts in a 20 *min* time window before CP onset. We choose 20 *min* rather  
 135 than the 10 *min* used by Kruse et al. (2022) since our temperature criterion involves a  
 136 minimum decrease of  $-0.5 K$  within 5 *min* to define the onset of potential CPs and might  
 137 thus delay the onset in comparison to Kruse et al. (2022). The 40 *min* time window af-  
 138 ter CP onset allows significant wind offsets while ensuring a temporal relation between  
 139  $\Delta T$  and  $\Delta u_g^{max}$ .

In case of missing wind gust anomalies between  $t-20 min$  and  $t+40 min$ , we iden-  
 tify the maximum wind gust,  $u_g^{max}$  within this time window rather than  $\Delta u_g^{max}$  and con-  
 sider the event a CP if

$$u_g^{max} \geq \bar{u}_g(t - 80 min) + 2 \sigma_{u_g}(t - 80 min). \quad (3)$$

140 By evaluating the centered 2-hour running mean  $\bar{u}_g$  and the corresponding stan-  
 141 dard deviation,  $\sigma_{u_g}$ , 80 *min* before CP onset, we keep again a 20 *min* offset between CP  
 142 onset and the 2-hour time window of the reference values. If no wind gust data has been  
 143 recorded between  $t - 20 min$  and  $t + 40 min$ , or if the reference values  $\bar{u}_g(t - 80 min)$   
 144 and  $\sigma_{u_g}(t - 80 min)$  could not be computed due to missing data, we consider the event  
 145 as "no CP."

146 Differing from Kruse et al. (2022), we evaluate the wind criterion based on wind  
 147 gust rather than wind speed. Since we work with station data with a temporal resolu-  
 148 tion of 5 *min* in contrast to 1 *min* in (Kruse et al., 2022), we find wind gust a better in-  
 149 dicator for CP gust fronts than wind speed.

150 **(iii) Duplicate detection check.** Often, a CP fulfills the defined criteria (i) and (ii)  
 151 not only at time  $t$ , but also at subsequent time steps. Depending on the evolution of tem-  
 152 perature and wind gust behind the CP gust front, time steps in which the criteria are  
 153 met can even be separated from each other by time steps in which the criteria are not  
 154 met. In order to avoid duplicate detection of a given CP, we drop detected CP events  
 155 if at least one other CP event was detected within 20 *min* before that particular event.  
 156 Given the variety of environmental conditions under which we observe CPs at our sta-  
 157 tion locations, we find this definition to be more permissive than the absolute 60 *min* time  
 158 window after detected temperature decreases, within which Kirsch et al. (2021) consider  
 159 any detected decrease as part of the same event.

### 160 3.2 Determination of Cold Pool Anomalies

161 We analyze the effects of a detected CP with respect to different station-measured  
 162 meteorological variables by considering a time window relative to CP onset,  $t_0$ , from  $t_0-$   
 163  $40 min$  to  $t_0+120 min$ . Within this time window, we evaluate the CP associated anom-  
 164 alies  $y'(t) \equiv y(t) - y_{ref}$  for a meteorological variable  $y$  based on an unperturbed refer-  
 165 ence state  $y_{ref}$ , which we define as the temporal mean of instantaneous measurements  
 166 in a time interval before CP onset. Since the onset is defined based on the temperature  
 167 drop and thus could be different for other variables, we choose the time interval from  $t_0-$   
 168  $40 min$  to  $t_0-20 min$  to keep a sufficient margin of 20 *min* to the CP onset while pre-  
 169 serving the required temporal proximity. To minimize any distortion of the reference state  
 170 through the diurnal cycle, we deviate from this definition only for temperature anom-  
 171 alies and follow the approach of the refined temperature drop from Kruse et al. (2022)  
 172 instead, i.e., we consider the maximum temperature of the two measurements in the 10 *min*  
 173 time window preceding the CP onset as unperturbed reference temperature.

174 Due to the coarser temporal resolution, we extend the time window in which we  
 175 analyze the anomalies before CP onset to 60 *min* for satellite-measured  $10.8 \mu m$  bright-

ness temperatures,  $BT_{10.8}$ , and define the reference brightness temperature,  $BT_{10.8}^{ref}$ , as the mean of the three observations in the time interval from  $t_0-60\text{ min}$  to  $t_0-30\text{ min}$ . As there might not be a brightness temperature observation at the station-derived CP onset,  $t_0$ , we define the closest satellite time step as  $\hat{t}_0$  and measure the CP time relative to it. The brightness temperature anomalies,  $BT'_{10.8}$ , are then computed analogously to those for station-measured variables. Moreover, to further investigate the space-borne CP signature, we additionally determine the temporal change of  $BT'_{10.8}$ , as  $\Delta BT'_{10.8}(t) = BT'_{10.8}(t) - BT'_{10.8}(t - 15\text{ min})$ .

## 184 4 Results

### 185 4.1 Seasonal and Diurnal Cycle of Observed Cold Pools

186 First, we derive the seasonal and diurnal cycles of CPs in the different sub-regions  
 187 (Fig. 1) and relate them with precipitation, convection depth and moisture conditions  
 188 (Fig. 2). With about 0.3–0.6 CPs per day in the high seasons (Fig. 2a, Table S2), equa-  
 189 torial Africa is a region with particular CP abundance compared to previous climatolo-  
 190 gies in other continental regions (Redl et al., 2015; Kirsch et al., 2021; Kruse et al., 2022).  
 191 In every sub-region, the number of CPs peaks twice during the course of the year with  
 192 a first maximum between March and May and a second maximum between September  
 193 and October. The bi-modality in the annual cycle of CPs largely corresponds to the lat-  
 194 itudinal migration of the Inter-Tropical Convergence Zone (ITCZ) which is reflected in  
 195 the precipitation seasonal cycles (Fig. 2c). However, we note that precipitation may not  
 196 explain all the features of the annual cycle of CPs and the differences between sub-regions.  
 197 For instance, Nigeria presents a single precipitation peak in September whereas the oc-  
 198 currence of CPs peaks in both May and September. There, the strong CP activity dur-  
 199 ing May may be related to the combination of deeper convection (Fig. 2e) fed by high  
 200 equivalent potential temperatures ( $\theta_E$ ; Fig. S1) and of higher low-level water vapor mix-  
 201 ing ratio deficit ( $r_D$ ; Fig. 2g) boosting rain evaporation. We also note that Uganda re-  
 202 ceives the least precipitation among sub-regions while experiencing the most of CPs dur-  
 203 ing the year. We attribute the larger number of CPs in Uganda to generally drier con-  
 204 ditions at low levels (Fig. 2g).

205 The diurnal cycle of CPs strongly peaks between 15 LT and 18 LT in most of the  
 206 regions with the exception of Nigeria where the peak is reached between 18 LT and 21 LT  
 207 (Fig. 2b). The high CP activity during the afternoon can be directly related to the af-  
 208 ternoon peak in (deep) convection, highlighted by maxima in precipitation (Fig. 2d) and  
 209 lower brightness temperatures (Fig. 2f). Consistently with earlier studies (Zhang et al.,  
 210 2016; Camberlin et al., 2018; Andrews et al., 2023), precipitation shows secondary noc-  
 211 turnal peaks in Uganda and Congo, and remains high during the night in Nigeria, whereas  
 212 the proportion of CPs displays local minima during these hours. This mismatch between  
 213 precipitation and CPs is likely to be related to both the decline of convection during the  
 214 night (leading to weaker rainfall intensities and downdrafts) and to moister conditions  
 215 at the surface (reducing rainfall evaporative cooling; Fig. 2h) which both inhibit CP for-  
 216 mation (Zuidema et al., 2017).

### 217 4.2 Observed Cold Pool Characteristics

218 We further characterize equatorial African CPs by examining their related temper-  
 219 ature and moisture anomalies (defined in Sec. 3.2). On average, a CP in equatorial Africa  
 220 is accompanied by a 5 K drop in temperature (compared to 3 K in Germany; Kirsch et  
 221 al. (2021)) occurring in about 30 minutes, with little variability among sub-regions (Fig. 3a,  
 222 Table S2). Different from Kirsch et al. (2021) over Germany, we generally observe a de-  
 223 crease in specific humidity after the passage of CPs over equatorial Africa (Fig. 3d). In-  
 224 terestingly, we find that the magnitude of this decrease is smaller in the elevated (Ta-  
 225 ble S1) stations of Uganda ( $-1\text{ g/kg}$ ) characterized by less deep convection (Fig. 2e,f)

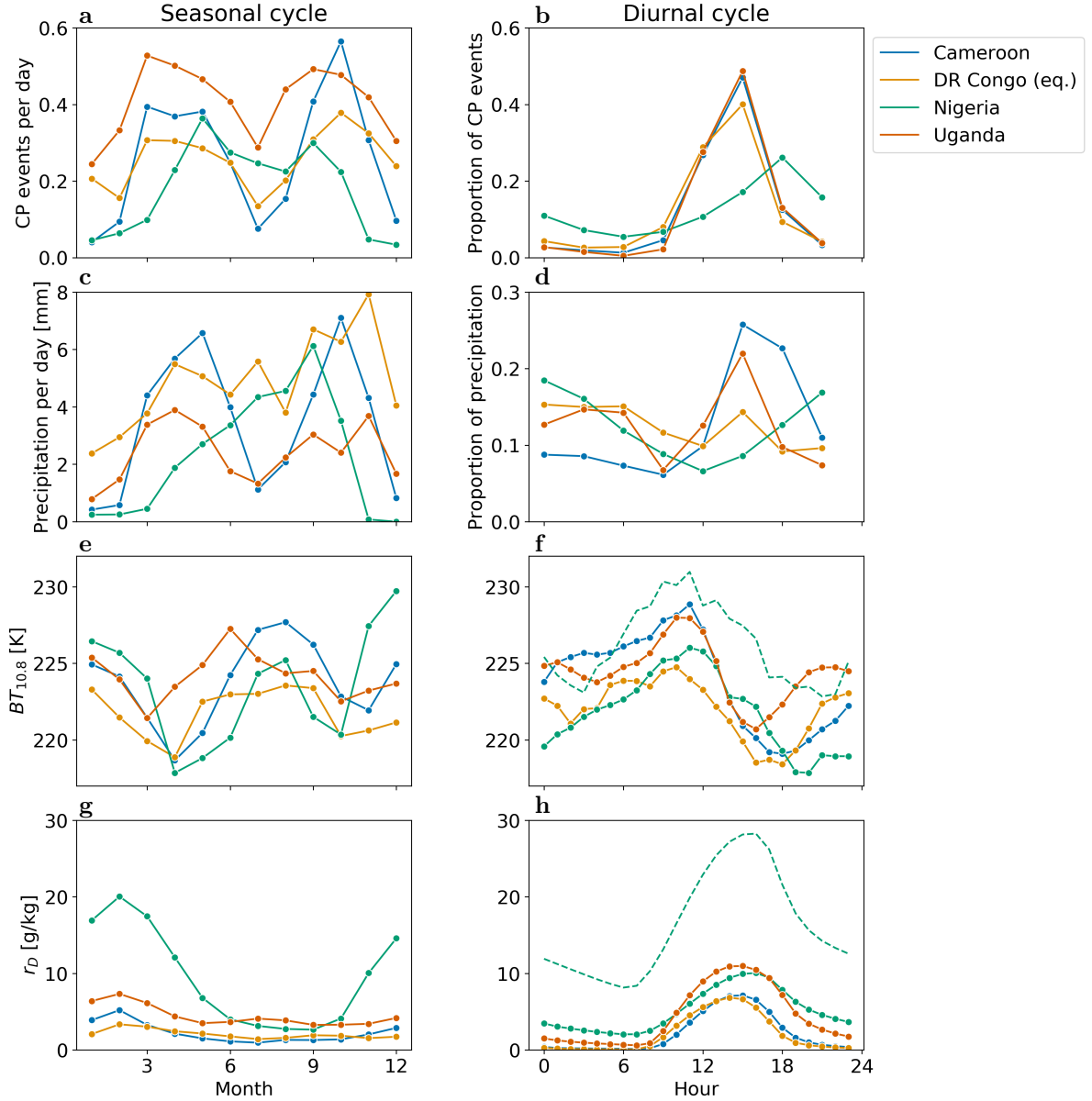


Figure 2: **Observed seasonal and diurnal cycles.** **a**, Mean number of daily cold pool (CP) events for each month. Lines interpolate linearly between markers to facilitate the interpretation; colors indicate different regions. The number of CP events is normalized based on the number of analyzed days per month and region. **b**, Proportion of CP events at different times of the day. Each marker represents the proportion of CP events observed within a given 3-hour time interval, starting with the interval [0,3) for the marker at 0 LT. Lines and colors analogous to (a). **c**, Analogous to (a) but for precipitation. **d**, Analogous to (b) but for precipitation. **e**, Mean  $10.8\ \mu\text{m}$  brightness temperature,  $BT_{10.8}$ , of deep clouds ( $BT_{10.8} \leq 240\ \text{K}$ ) for each month. Lines and colors analogous to (a). **f**, Mean  $BT_{10.8}$  of deep clouds at different times of the day. Intervals, lines and colors analogous to (b). The two lines for Nigeria represent rainy months (Apr–Oct, solid line with markers) and dry months (Nov–Mar, dashed). **g**, Analogous to (e) but for mean mixing ratio deficit,  $r_D$ . **h**, Analogous to (f) but for mean  $r_D$ .

226 and drier low-level environments (Fig. 2g,h) compared to the other sub-regions (about  
 227  $-3\text{ g/kg}$ ). Less deep convection is likely to be associated with less elevated (relative to  
 228 the surface level) convective downdrafts (Zuidema et al., 2017) importing less upper-level  
 229 dry air to the surface, which combined with enhanced rain evaporation due to drier en-  
 230 vironments, may explain the reduced decline in specific humidity over Uganda. When  
 231 considering the 25% driest (moistest) low-level pre-CP environments, we further evidence  
 232 the large impact of moisture conditions, and thus of rain evaporation, on CP temper-  
 233 ature and moisture anomalies in all sub-regions (Fig. 2b,c,e,f). Indeed, we find CP anom-  
 234 alies that are on average  $3\text{ K}$  cooler and  $2\text{ g/kg}$  moister in the driest pre-CP conditions  
 235 than in the moistest pre-CP conditions. We note weak maxima in specific humidity occur-  
 236 ring few minutes after the CP onset (so-called moisture rings) over Cameroon, Uganda  
 237 and Congo for the driest pre-CP environments. Finally, the temporal evolutions of  $r_D$   
 238 (Fig. 3g,h,i) reveal that in the driest environments, rain evaporation is not sufficient to  
 239 saturate the low-level air (similar to Germany; Kirsch et al. (2021)).

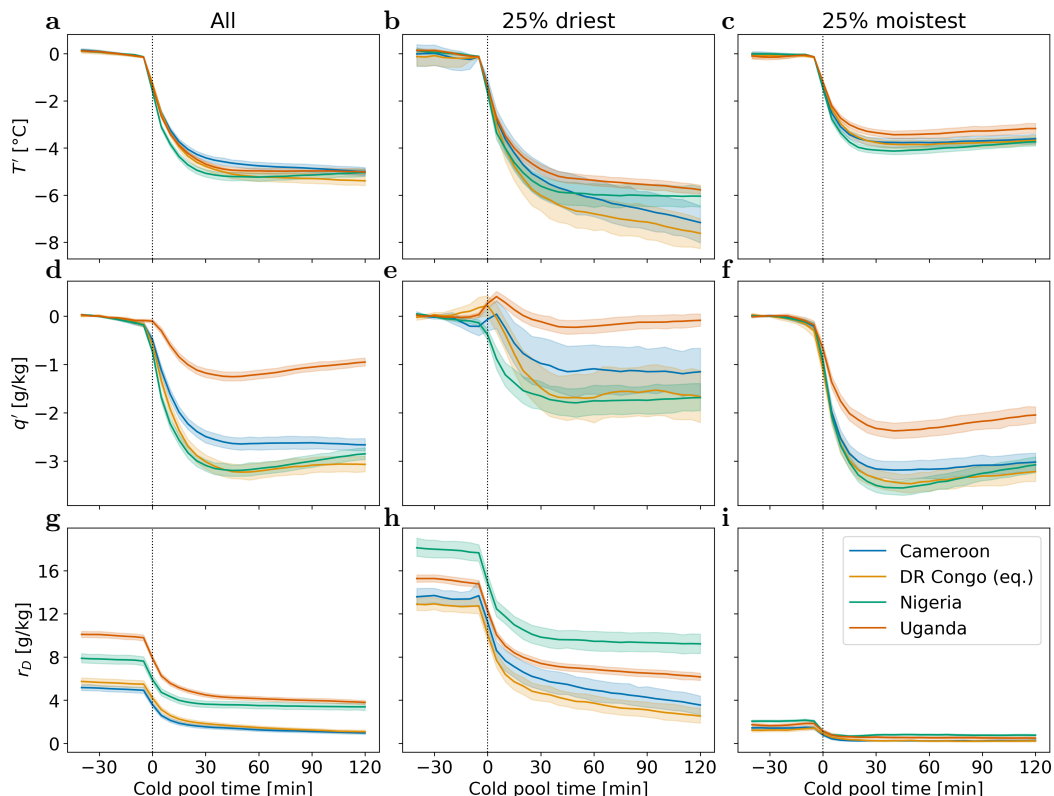


Figure 3: **Station-derived cold pool (CP) properties relative to CP onset,  $t_0$ .** **a**, Mean temperature anomalies,  $T'$ , for different regions; shading indicates the 95% confidence interval. **b**, Analogous to (a) but for the 25% driest CPs of each region w.r.t. the reference mixing ratio deficit,  $r_D^{ref}$ , prior to  $t_0$ . **c**, Analogous to (b) but for the 25% moistest CPs. **d–f**, Analogous to (a)–(c) but for mean specific humidity anomalies,  $q'$ . **g–i**, Analogous to (a)–(c) but for mean mixing ratio deficits,  $r_D$ . Note that only timeseries of CPs, where  $t_0$  is more than 120 minutes apart from other CP onsets, are included in the analysis.

240 Moving to CP cloud characteristics, we find that 92% (Nigeria) to 100% (Congo)  
 241 of CP gust fronts are accompanied by shallow or deep convective clouds (Fig. S2a). More  
 242 specifically, a CP is generally accompanied by a strong (reaching  $30\text{ K}$  in Cameroon) de-  
 243 crease in  $BT_{10.8}$  (Fig. 4a). The  $BT_{10.8}$  minimum is typically reached 30–45 minutes af-

244 ter CP onset. While this minimum is delayed w.r.t. the CP onset, we find a minimum  
 245 of the time derivative of  $BT'_{10.8}$  synchronized with the CP onset in all sub-regions (Fig. 4b).  
 246 This observation suggests that CPs in equatorial Africa, and potentially other regions,  
 247 might be detectable from space-borne satellite data.

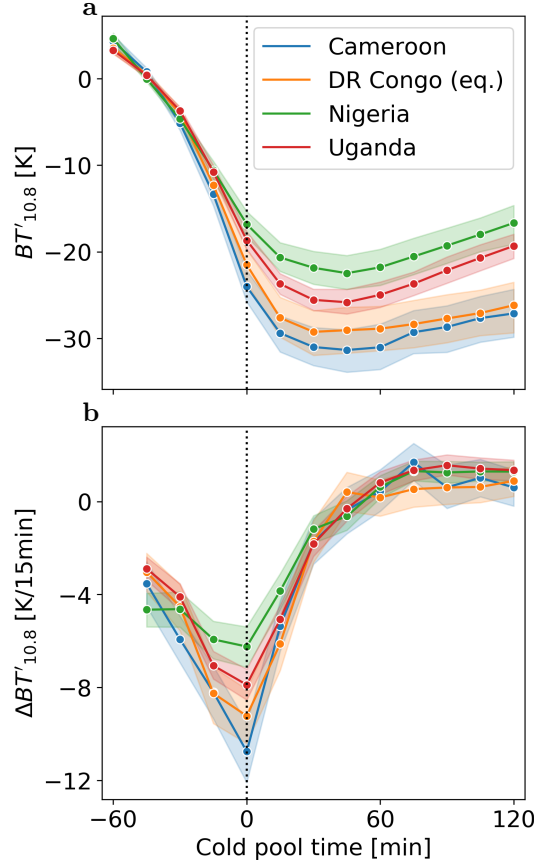


Figure 4: **Space-borne signatures of cold pools (CPs) relative to CP onset,  $\hat{t}_0$ .**  
**a**, Mean  $10.8\mu m$  brightness temperature anomalies,  $BT'_{10.8}$ , of station-derived CPs for  
 different regions; shading indicates the 95% confidence interval. **b**, Analogous to (a) but  
 for the corresponding derivative  $\Delta BT'_{10.8}$ .

248 **4.3 Cold Pool Examples With Deep and Shallow Convection**

249 We now turn to two contrasting examples of observed CPs (Fig. 5). The two sta-  
 250 tion locations at which the CPs were detected are indicated in Fig. 5a).

251 The first CP (Fig. 5; left column) was detected in DR Congo at station TA673 on  
 252 November 28, 2021, at 13:40 UTC. The CP was associated with a mesoscale convective  
 253 system, visible in the satellite-derived  $10.8\mu m$  brightness temperature image at 13:45  
 254 UTC (Fig. 5b). The corresponding brightness temperature timeseries of different satel-  
 255 lite channels at the station are depicted in Fig. 5d). All channels show a significant bright-  
 256 ness temperature decrease around CP onset, with a maximum decrease rate right at the  
 257 onset. Between 12:30 and 14:45 UTC, the brightness temperature dropped by  $85 K$  in  
 258 the  $10.8\mu m$  channel and then slowly increased again. The station record (Fig. 5f) fur-  
 259 ther reveals a massive air temperature drop of  $9.6 K$  between 13:40 and 14:00 UTC, ac-  
 260 companied by increased wind gust speeds of up to  $6.5 m/s$ . By 14:00 UTC, when the tem-

261 perature stabilized again, the air became fully saturated. Five minutes later, the rain-  
 262 fall intensity peaked at approximately  $65\text{ mm/h}$ .

263 The second CP (Fig. 5; right column) was detected in Uganda at station TA222  
 264 on July 2, 2021, at 12:05 UTC. During the time it was detected, the CP featured arc-  
 265 shaped shallow convection at the gust front, distinctly separated from the parent con-  
 266 vection by clear skies (Fig. 5c). The corresponding brightness temperature timeseries at  
 267 the station (Fig. 5e) confirm the passage of low-level clouds right at the time of the station-  
 268 derived CP onset. Around the CP onset, no rainfall was measured at the station (Fig. 5g).  
 269 This time, the observed wind gust speeds increase approximately 5–10 minutes before  
 270 the drop in air temperature and reach a peak value of  $10\text{ m/s}$  at CP onset.

## 271 5 Summary and Discussion

272 The present study provides multi-year statistics of cold pool characteristics in equa-  
 273 torial Africa, based on five-minute near-surface weather data. Using detection methods  
 274 similar to those in previous studies focused on mid-latitude continental regions, key find-  
 275 ings include that temperature drops upon gust front passage often exceed  $5\text{ K}$  and spe-  
 276 cific humidities typically decrease by more than  $3\text{ g/kg}$ . Weak moisture rings can only  
 277 be identified for the driest cold pools in some of the regions — in agreement with Kruse  
 278 et al. (2022) for data in the Netherlands where moisture rings were generally not detected.

279 Seasonally, the rate of cold pool occurrence roughly follows precipitation statistics.  
 280 Yet, diurnally, the fact that the nocturnal boundary layer is often close to saturation may  
 281 focus the diurnal cycle of cold pool occurrence on the drier late afternoon times. This  
 282 may have important implications for thunderstorm organization through cold pool ac-  
 283 tivity: the limited time window where cold pools actually occur during the day means  
 284 that self-organization may be limited to relatively short periods of the day. One could  
 285 speculate that it is the lack of cold pool activity that limits the duration of mesoscale  
 286 convective systems, often less than 12 hours, rather than the precipitation itself (which  
 287 is more spread out over the day). Future studies should analyze if deep convection is more  
 288 scattered during the nocturnal periods when fewer cold pools occur. Comparisons with  
 289 oceanic cold pools and their organizational effects, which tend to be weaker (Zuidema  
 290 et al., 2017), would be useful.

291 Our cold pool detection algorithm can be adapted to other regions, provided that  
 292 there are in-situ weather stations measuring surface wind and temperature with at least  
 293 a 5-minute temporal resolution. However, in-situ weather stations meeting this require-  
 294 ment are still limited in the tropics, whereas cold pools are abundant. Encouragingly,  
 295 our findings may have implications for satellite-based cold pool detection: we show that  
 296 the gust front passage clearly correlates with discontinuities in satellite-derived bright-  
 297 ness temperature. We generally observe a significant decrease in brightness temperatures  
 298 around the time of the gust front passage, with maximum decrease rates at the station-  
 299 derived cold pool onset. Our findings thus suggest that cold pools in equatorial Africa,  
 300 and potentially other regions, could be directly detectable from geostationary satellite  
 301 data on a continental scale. Even in cases where not all parts of a cold pool gust front  
 302 exhibit brightness temperature drops (Fig. S2b), neural networks, such as those devel-  
 303 oped by Hoeller, Fiévet, and Haerter (2023), may still possess the capability to detect  
 304 the overall two-dimensional pattern and accurately track the gust front.

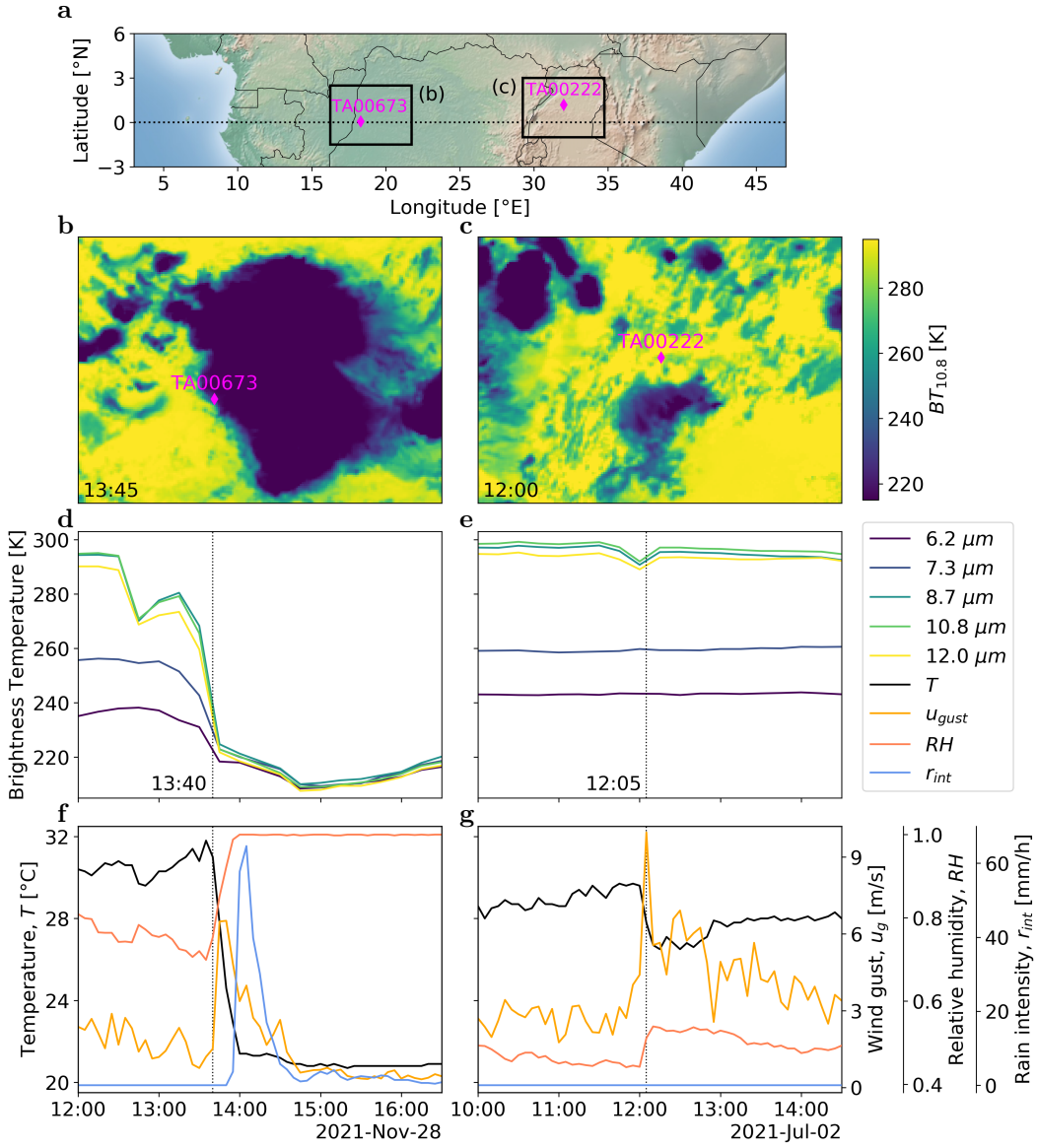


Figure 5: **Cold pool (CP) case studies.** **a**, Map displaying the locations of the stations utilized in the two case studies. Rectangles indicate the regions depicted in (b) and (c). **b**, Satellite-derived  $10.8\mu\text{m}$  brightness temperatures,  $BT_{10.8}$ , in the vicinity of station TA00673 on November 28, 2021, at 13:45, close to a station-derived CP onset at 13:40. **c**, Analogous to (b) but for station TA00222 on July 2, 2021, at 12:00 and a CP onset at 12:05. **d**, Timeseries of satellite-derived brightness temperatures at station TA00673 during the CP event visualized in (b). **e**, Analogous to (d) but for the CP event at station TA00222 visualized in (c). **f-g**, Analogous to (d-e) but for different near-surface observations.

## 305 Data Availability Statement

306 Both the code for the cold pool gust front identification and the processed data sets  
 307 are licensed under Creative Commons Attribution 4.0 International and were used in ver-  
 308 sion 1.0 (Hoeller, Haerter, & Silva, 2023). The raw data of the automatic weather sta-  
 309 tions was provided by TAHMO (TAHMO, 2023) and is not publicly available. Interested  
 310 parties may contact info@tahmo.org for this data. The satellite-observed radiances were  
 311 extracted from Meteosat Second Generation (MSG) 0° products, provided by EUMET-  
 312 SAT without a licence on an unrestricted basis (EUMETSAT, 2023). Figures were made  
 313 with Matplotlib version 3.5.2 (Hunter, 2007; Caswell et al., 2022) and seaborn version  
 314 0.12.2 (Waskom, 2021).

## 315 Conflicts of Interest Statement

316 The authors have no conflicts of interest to declare.

## 317 Acknowledgments

318 The authors gratefully acknowledge funding by a grant from the VILLUM Foundation  
 319 (grant number: 13168) and the European Research Council (ERC) under the European  
 320 Union’s Horizon 2020 research and innovation program (grant number: 771859) and the  
 321 Novo Nordisk Foundation Interdisciplinary Synergy Program (grant no. NNF19OC0057374).  
 322 This work used resources of the Deutsches Klimarechenzentrum (DKRZ), granted by its  
 323 Scientific Steering Committee (WLA) under project ID bb1166. Additionally, the au-  
 324 thors thank the Trans-African Hydro-Meteorological Observatory (TAHMO) for the pro-  
 325 vision of meteorological data. Interested parties may contact info@tahmo.org for these  
 326 data.

## 327 References

- 328 Adams, D. K., Fernandes, R. M., Holub, K. L., Gutman, S. I., Barbosa, H. M.,  
 329 Machado, L. A., ... others (2015). The amazon dense gns meteorological  
 330 network: A new approach for examining water vapor and deep convection  
 331 interactions in the tropics. *Bulletin of the American Meteorological Society*,  
 332 *96*(12), 2151–2165.
- 333 Andrews, P. C., Cook, K. H., & Vizi, E. K. (2023). Mesoscale convective systems in  
 334 the congo basin: seasonality, regionality, and diurnal cycles. *Climate Dynam-*  
 335 *ics*, 1–22. doi: 10.1007/s00382-023-06903-7
- 336 Böing, S. J. (2016). An object-based model for convective cold pool dynamics. *Math-*  
 337 *ematics of Climate and Weather Forecasting*, *2*(1).
- 338 Camberlin, P., Gitau, W., Planchon, O., Dubreuil, V., Funatsu, B. M., & Philip-  
 339 pon, N. (2018). Major role of water bodies on diurnal precipitation regimes  
 340 in eastern africa. *International Journal of Climatology*, *38*(2), 613–629. Re-  
 341 trieved from [https://rmets.onlinelibrary.wiley.com/doi/abs/10.1002/](https://rmets.onlinelibrary.wiley.com/doi/abs/10.1002/joc.5197)  
 342 [joc.5197](https://doi.org/10.1002/joc.5197) doi: <https://doi.org/10.1002/joc.5197>
- 343 Caswell, T. A., Droettboom, M., Lee, A., de Andrade, E. S., Hoffmann, T., Klymak,  
 344 J., ... Ivanov, P. (2022). *matplotlib/matplotlib: Release (version 3.5.2) [soft-*  
 345 *ware]*. Zenodo. Retrieved from <https://doi.org/10.5281/zenodo.6513224>  
 346 doi: 10.5281/zenodo.6513224
- 347 Chandra, A. S., Zuidema, P., Krueger, S., Kochanski, A., de Szoeko, S. P., & Zhang,  
 348 J. (2018). Moisture distributions in tropical cold pools from equatorial indian  
 349 ocean observations and cloud-resolving simulations. *Journal of Geophysical*  
 350 *Research: Atmospheres*, *123*(20), 11–445.
- 351 Drager, A. J., Grant, L. D., & van den Heever, S. C. (2020). Cold pool responses  
 352 to changes in soil moisture. *Journal of Advances in Modeling Earth Systems*,

- 12(8), e2019MS001922.
- 353 Engerer, N. A., Stensrud, D. J., & Coniglio, M. C. (2008). Surface characteristics of  
354 observed cold pools. *Monthly Weather Review*, *136*(12), 4839–4849.
- 355 EUMETSAT. (2012). *The conversion from effective radiances to equivalent bright-*  
356 *ness temperatures (version 1)*. Retrieved from [https://www-cdn.eumetsat](https://www-cdn.eumetsat.int/files/2020-04/pdf_effect_rad_to_brightness.pdf)  
357 [.int/files/2020-04/pdf\\_effect\\_rad\\_to\\_brightness.pdf](https://www-cdn.eumetsat.int/files/2020-04/pdf_effect_rad_to_brightness.pdf)
- 358 EUMETSAT. (2023). *Meteosat second generation (msg) high rate seviri level 1.5*  
359 *image data - 0 degree [dataset]*. Retrieved from [https://navigator.eumetsat](https://navigator.eumetsat.int/product/EO:EUM:DAT:MSG:HRSEVIRI)  
360 [.int/product/EO:EUM:DAT:MSG:HRSEVIRI](https://navigator.eumetsat.int/product/EO:EUM:DAT:MSG:HRSEVIRI)
- 361 Feng, Z., Hagos, S., Rowe, A. K., Burleyson, C. D., Martini, M. N., & de Szoeke,  
362 S. P. (2015). Mechanisms of convective cloud organization by cold pools over  
363 tropical warm ocean during the amie/dynamo field campaign. *Journal of*  
364 *Advances in Modeling Earth Systems*, *7*(2), 357–381.
- 365 Fiévet, R., Meyer, B., & Haerter, J. O. (2022). On the sensitivity of convective cold  
366 pools to mesh resolution. *Earth and Space Science Open Archive*, *24*. Re-  
367 trieved from <https://doi.org/10.1002/essoar.10512297.1> doi: 10.1002/  
368 [essoar.10512297.1](https://doi.org/10.1002/essoar.10512297.1)
- 369 Fournier, M. B., & Haerter, J. O. (2019). Tracking the gust fronts of convective cold  
370 pools. *Journal of Geophysical Research: Atmospheres*, *124*(21), 11103–11117.
- 371 Gentine, P., Garelli, A., Park, S., Nie, J., Torri, G., & Kuang, Z. (2016). Role of sur-  
372 face heat fluxes underneath cold pools. *Geophys. Res. Lett.*, *43*, 874–883. doi:  
373 [10.1002/2015gl067262](https://doi.org/10.1002/2015gl067262)
- 374 Haerter, J. O. (2019). Convective self-aggregation as a cold pool-driven critical phe-  
375 nomenon. *Geophysical Research Letters*, *46*(7), 4017–4028. doi: [https://doi](https://doi.org/10.1029/2018GL081817)  
376 [.org/10.1029/2018GL081817](https://doi.org/10.1029/2018GL081817)
- 377 Haerter, J. O., Böing, S. J., Henneberg, O., & Nissen, S. B. (2019). Circling in on  
378 convective organization. *Geophysical Research Letters*, *46*(12), 7024–7034. doi:  
379 <https://doi.org/10.1029/2019GL082092>
- 380 Haerter, J. O., Meyer, B., & Nissen, S. B. (2020). Diurnal self-aggregation. *npj Cli-*  
381 *mate and Atmospheric Science*, *3*. doi: [10.1038/s41612-020-00132-z](https://doi.org/10.1038/s41612-020-00132-z)
- 382 Henneberg, O., Meyer, B., & Haerter, J. O. (2020). Particle-based tracking of cold  
383 pool gust fronts. *J. Adv. Model. Earth Syst.*, *12*. doi: [10.1029/2019ms001910](https://doi.org/10.1029/2019ms001910)
- 384 Hitchcock, S. M., Schumacher, R. S., Herman, G. R., Coniglio, M. C., Parker, M. D.,  
385 & Ziegler, C. L. (2019). Evolution of pre-and postconvective environmental  
386 profiles from mesoscale convective systems during pecan. *Monthly Weather*  
387 *Review*, *147*(7), 2329–2354.
- 388 Hoeller, J., Fiévet, R., & Haerter, J. O. (2022). U-net segmentation for the detection  
389 of convective cold pools from cloud and rainfall fields. *Authorea Preprints*.
- 390 Hoeller, J., Fiévet, R., & Haerter, J. O. (2023). Detecting cold pool family trees in  
391 convection resolving simulations. *Authorea Preprints*.
- 392 Hoeller, J., Haerter, J. O., & Silva, N. D. (2023). *Identification algorithm for cold*  
393 *pool gust fronts in weather station data from equatorial africa (version 1.0)*  
394 *[software & dataset]*. Zenodo. Retrieved from [https://doi.org/10.5281/](https://doi.org/10.5281/zenodo.10117789)  
395 [zenodo.10117789](https://doi.org/10.5281/zenodo.10117789) doi: [10.5281/zenodo.10117789](https://doi.org/10.5281/zenodo.10117789)
- 396 Hunter, J. D. (2007). Matplotlib: A 2d graphics environment [software]. *Computing*  
397 *in Science & Engineering*, *9*(3), 90–95. doi: [10.1109/MCSE.2007.55](https://doi.org/10.1109/MCSE.2007.55)
- 398 Jensen, G. G., Fiévet, R., & Haerter, J. O. (2021). The diurnal path to persistent  
399 convective self-aggregation. *arXiv preprint arXiv:2104.01132*.
- 400 Kirsch, B., Ament, F., & Hohenegger, C. (2021). Convective cold pools in long-term  
401 boundary layer mast observations. *Monthly Weather Review*, *149*(3), 811–820.
- 402 Kruse, I. L., Haerter, J. O., & Meyer, B. (2022). Cold pools over the netherlands:  
403 A statistical study from tower and radar observations. *Quarterly Journal of the*  
404 *Royal Meteorological Society*, *148*(743), 711–726.
- 405 Langhans, W., & Romps, D. M. (2015). The origin of water vapor rings in tropical  
406 oceanic cold pools. *Geophysical Research Letters*, *42*(18), 7825–7834.
- 407

- 408 Meyer, B., & Haerter, J. O. (2020, 11). Mechanical forcing of convection by cold  
 409 pools: Collisions and energy scaling. *J. Adv. Model. Earth Syst.*, *12*(11), n/a–  
 410 n/a. Retrieved from [https://doi.org/10.1029/  
 411 2020MS002281](https://doi.org/10.1029/2020MS002281) doi: 10.1029/  
 412 Mueller, C. K., & Carbone, R. E. (1987). Dynamics of a thunderstorm outflow.  
 413 *Journal of the Atmospheric sciences*, *44*(15), 1879–1898.  
 414 Niehues, J., Jensen, G. G., & Haerter, J. O. (2022). Self-organized quantization and  
 415 oscillations on continuous fixed-energy sandpiles. *Physical Review E*, *105*(3),  
 416 034314.  
 417 Nissen, S. B., & Haerter, J. O. (2021). Circling in on convective self-aggregation.  
 418 *Journal of Geophysical Research: Atmospheres*, *126*(20), e2021JD035331.  
 419 Parker, D. J., Fink, A., Janicot, S., Ngamini, J.-B., Douglas, M., Afiesimama, E.,  
 420 ... others (2008). The amma radiosonde program and its implications for  
 421 the future of atmospheric monitoring over africa. *Bulletin of the American  
 422 Meteorological Society*, *89*(7), 1015–1028.  
 423 Purdom, J. F. (1976). Some uses of high-resolution goes imagery in the mesoscale  
 424 forecasting of convection and its behavior. *Monthly Weather Review*, *104*(12),  
 425 1474–1483.  
 426 Redl, R., Fink, A. H., & Knippertz, P. (2015). An objective detection method for  
 427 convective cold pool events and its application to northern africa. *Monthly  
 428 Weather Review*, *143*(12), 5055–5072.  
 429 Simpson, J. (1980). Downdrafts as linkages in dynamic cumulus seeding effects.  
 430 *Journal of Applied Meteorology*, *19*(4), 477–487.  
 431 TAHMO. (2023). *Trans-african hydro-meteorological observatory (tahmo) weather  
 432 station data [dataset]*. Retrieved from [https://tahmo.org/climate-data/  
 433 Tompkins, A. M. \(2001a\). Organization of tropical convection in low vertical wind  
 434 shears: The role of cold pools. \*Journal of the Atmospheric Sciences\*, \*58\*, 1650–  
 435 1672. doi: 10.1175/1520-0469\(2001\)058<1650:ootcil>2.0.co;2  
 436 Tompkins, A. M. \(2001b\). Organization of tropical convection in low vertical wind  
 437 shears: The role of water vapor. \*Journal of the Atmospheric Sciences\*, \*58\*\(6\),  
 438 529–545.  
 439 Torri, G., & Kuang, Z. \(2019\). On cold pool collisions in tropical boundary layers.  
 440 \*Geophys. Res. Lett.\*, \*46\*, 399–407. doi: 10.1029/2018gl080501  
 441 Torri, G., Kuang, Z., & Tian, Y. \(2015\). Mechanisms for convection triggering by  
 442 cold pools. \*Geophysical Research Letters\*, \*42\*\(6\), 1943–1950.  
 443 van de Giesen, N., Hut, R., & Selker, J. \(2014\). The trans-african hydro-  
 444 meteorological observatory \(tahmo\). \*Wiley Interdisciplinary Reviews: Water\*,  
 445 \*1\*\(4\), 341–348.  
 446 van den Heever, S. C., Grant, L. D., Freeman, S. W., Marinescu, P. J., Barnum, J.,  
 447 Bukowski, J., ... others \(2021\). The colorado state university convective cloud  
 448 outflows and updrafts experiment \(c 3 loud-ex\). \*Bulletin of the American  
 449 Meteorological Society\*, \*102\*\(7\), E1283–E1305.  
 450 Vogel, R. \(2017\). \*The influence of precipitation and convective organization on the  
 451 structure of the trades\* \(Unpublished doctoral dissertation\). Universität Ham-  
 452 burg Hamburg.  
 453 Vogel, R., Konow, H., Schulz, H., & Zuidema, P. \(2021\). A climatology of trade-  
 454 wind cumulus cold pools and their link to mesoscale cloud organization. \*Atmo-  
 455 spheric Chemistry and Physics\*, \*21\*\(21\), 16609–16630.  
 456 Wakimoto, R. M. \(1982\). The life cycle of thunderstorm gust fronts as viewed  
 457 with doppler radar and rawinsonde data. \*Monthly weather review\*, \*110\*\(8\),  
 458 1060–1082.  
 459 Waskom, M. L. \(2021\). seaborn: statistical data visualization \[software\]. \*Jour-  
 460 nal of Open Source Software\*, \*6\*\(60\), 3021. Retrieved from \[https://doi.org/  
 461 10.21105/joss.03021\]\(https://doi.org/10.21105/joss.03021\) doi: 10.21105/joss.03021  
 462 Zhang, G., Cook, K. H., & Vizy, E. K. \(2016\). The diurnal cycle of warm season](https://tahmo.org/climate-data/)

- 463 rainfall over west africa. part i: Observational analysis. *Journal of Climate*,  
464 29(23), 8423 - 8437. doi: 10.1175/JCLI-D-15-0874.1
- 465 Zipser, E. (1977). Mesoscale and convective-scale downdrafts as distinct components  
466 of squall-line structure. *Monthly Weather Review*, 105(12), 1568–1589.
- 467 Zuidema, P., Li, Z., Hill, R. J., Bariteau, L., Rilling, B., Fairall, C., . . . Hare, J.  
468 (2012). On trade wind cumulus cold pools. *Journal of the Atmospheric Sci-*  
469 *ences*, 69(1), 258–280.
- 470 Zuidema, P., Torri, G., Muller, C., & Chandra, A. (2017). A survey of precipitation-  
471 induced atmospheric cold pools over oceans and their interactions with the  
472 larger-scale environment. *Surveys in Geophysics*, 1–23.

### 473 **References From the Supporting Information**

- 474 Bolton, D. (1980). The computation of equivalent potential temperature. *Monthly*  
475 *weather review* , 108 (7), 1046–1053.
- 476 Wallace, J. M., & Hobbs, P. V. (2006). *Atmospheric science: an introductory survey*  
477 (Vol. 92). Elsevier.